

Three-Dimensional CFD Simulation Coupled with Thermal Contraction in Direct-Chill Casting of A390 Aluminum Alloy Hollow Billet



KESHENG ZUO, HAITAO ZHANG, KE QIN, JIANZHONG CUI,
and QINGZHANG CHEN

A three-dimensional CFD model coupled with melt flow, heat transfer, and thermal contraction was developed to simulate the direct-chill (DC) casting process of A390 alloy hollow billet with a cross-section size of $\Phi 164$ mm/ $\Phi 60$ mm. This study considered the effects of contact height and air gap width between the core and the hollow billet, which dominated the heat transfer at the inner wall of the hollow billet. The effects of core taper angle, relative vertical position of core in the mold, and casting speed on the steady-state temperature distribution and formability of hollow billet were investigated. According to the criterion used in this study, the optimal core taper angle is 3 deg for DC casting of A390 alloy hollow billet. With the optimal core taper angle, the A390 alloy hollow billet can be cast successfully regardless of the variation of the relative vertical position of core in the mold and casting speed. The coupled model developed in this study can be applied to optimize the core taper angle and study the effects of casting parameters in various dimensions of hollow billet.

DOI: 10.1007/s11663-016-0857-9

© The Minerals, Metals & Materials Society and ASM International 2016

I. INTRODUCTION

THE direct-chill (DC) casting process is being used widely to produce extrusion billets and rolling slabs of aluminum alloys due to its relative simplicity and robust nature.^[1] When pipes are to be produced *via* mandrel extrusion, the extrusion billets are preferred to be in hollow shape for the purpose of ease of operation and high yield. A schematic of the DC casting process for hollow billet is shown in Figure 1. This process is similar to the DC casting process for solid billets except that it contains a water-cooled inner mold (often made of copper). The molten metal is horizontally fed from the delivery system into the cavity surrounded by the hot top, core hot top, mold, inner mold (Cu core), and starting block. After the molten metal is cooled by the mold or Cu core, the initial solid shells would form at the outer and inner walls of hollow billet. As soon as the solid shells are strong enough to embay the interior molten metal, the starting block is translated downward together with the solid shell. As the starting block exits the bottom of mold, the outer wall of hollow billet is cooled rapidly by a direct flow of water. However, a macroscopic air gap forms once the inner wall of hollow

billet is separated from the outer wall of Cu core. The heat dissipation at the inner wall is dominated by the surrounding air. This process terminates when the hollow billet with a desired height is obtained. The hollow billet can be then sectioned, homogenized, and hot extruded to produce pipes.

Except for the adjustments of conventional casting parameters, such as casting speed, casting temperature, and cooling water flow rate, the formability of hollow billet largely depends upon the design of taper angle of the Cu core (θ). An appropriate core taper angle should be designed to ensure the success of DC casting process for hollow billet. Because the diameters of both the outer and the inner walls decrease as the solid shells shrink during the DC casting process. If the core taper angle is smaller than the certain value, the shrinking inner solid wall of hollow billet would directly contact with the outer wall of the core. The excessive contact pressure propels the core to be drawn into the hollow billet and leads to the occurrence of “hanging” problem. However, when the core taper angle is too large, which would enlarge the air gap width between the core and hollow billet, leading to partial remelting of the inner wall and the formation of liquid metal exudation, the extreme case is that the interior molten metal breaks out. Therefore, it is crucial to investigate the DC casting process for hollow billet and a suitable core taper angle should be determined. Numerous numerical simulations have been carried out to gain a better understanding of the DC casting process and optimize the process parameters.^[2–6] For this purpose, a mathematical model is required to analyze the DC casting process for hollow billet and optimize the core taper angle. The challenge in establishing this model is the requirement to couple the

KESHENG ZUO, Lecturer, and QINGZHANG CHEN, Professor, are with the School of Automotive Engineering, Changshu Institute of Technology, Changshu 215500, China. Contact e-mail: zuoks163@163.com HAITAO ZHANG and KE QIN, Associate Professors, and JIANZHONG CUI, Professor, are with the Key Laboratory of Electromagnetic Processing of Materials, Ministry of Education, Northeastern University, Shenyang 110819, China.

Manuscript submitted June 21, 2016.

Article published online November 23, 2016.

fluid flow and thermal contraction of solid shell during the DC casting process. This is why the simulation of DC casting process for hollow billet has not yet been realized ever before.

As studied by some researchers,^[7,8] two stages exist before the formation of macroscopic air gap within the primary cooling zone. When the metal is totally liquid, the melt is in good contact with the mold. The heat transfer coefficient (HTC) is relatively high and mainly depends upon the surface roughness. With the temperature of molten metal decreasing below the liquidus temperature, the HTC decreases gradually because the partial solidification deteriorates the contact state between the mold and the melt. A macroscopic air gap forms until the solid shell is strong enough to withstand the metallostatic pressure.

As experimentally studied by some researchers,^[9,10] the HTC is inversely proportional to the air gap size. Several methods have been proposed to predict the air gap size between the mold and the casting. Verwijs and Weckman^[11] developed a thermoelastic model to predict the air gap size and mold boundary conditions during the horizontal DC casting process of rods. Huang *et al.*^[12] developed the free thermal contraction method to describe the variation and distribution of the air gap width. Chow *et al.*^[13] predicted the HTC by modeling the air gap based on solving the coupled problem of solidification and thermal stress analysis. Baserinia *et al.*^[14,15] developed a simple density-based model to predict the air gap size during the DC casting of rectangular ingots. Unfortunately, the proposed model is limited to application in solid billet because the thermal contraction direction is constrained merely toward the interior.

The primary objective of this study was to develop an accurate predictive model that can be used to estimate the contact height and HTC between the core and

hollow billet during the DC casting process. Such a model includes the effect of contact height and air gap width between the core and solid shell, which is, for the first time, applied during the DC casting process of hollow billet. With this model, the optimal core taper angle was obtained and the effects of casting parameters on heat transfer, solidification, and thermal contraction were investigated.

II. MATHEMATICAL MODEL

A hollow billet with a cross-section size of $\Phi 164$ mm/ $\Phi 60$ mm and a length of 2000 mm was simulated. Due to the symmetry, only half of the hollow billet was used in this work. For the purpose of better visualization of the simulation settings and results, only one-eighth of the hollow billet in the casting direction is magnified. The computational domain for the melt flow and temperature field is shown in Figure 2. The origin of the computational domain is at $x = 0, y = 0, z = 0$ at the upper edge of mold.

A. Governing Equations

The model for the heat and melt flow is based on the continuum mixture model for the solid-liquid material by Bennon and Incropera.^[16,17] This single-domain method treated liquid, mushy, and solid regions as one continuous region. These regions were implicitly defined

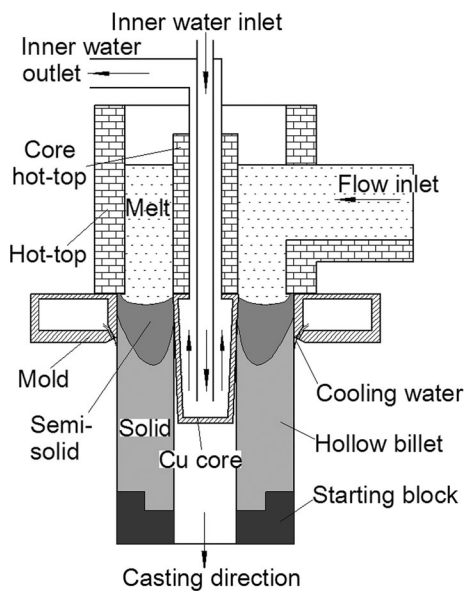


Fig. 1—Schematic of a DC caster for hollow billet.

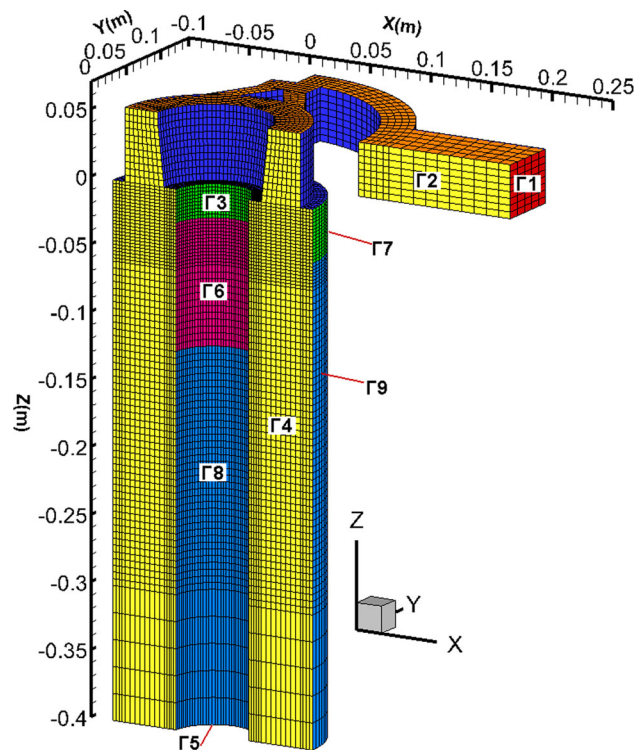


Fig. 2—Computational domain of the DC cast hollow billet. $\Gamma 1$ through $\Gamma 10$ correspond to the boundary conditions defined in the main text.

within this system by the distributions of energy determined by the model equations. The following assumptions are invoked:

- An incompressible Newtonian fluid is assumed. But thermal convection is included by Boussinesq approximation.
- The calculation of the solute field is not included in this model and Si particles are assumed to have the same velocity as the surrounding melt.
- The effect of exudation of liquid metal on the air gap width is ignored at the outer and inner walls of hollow billet.
- Only the steady state of DC casting process is modeled without taking into account the start-up condition.
- The plastic strain is neglected in the hollow billet during the DC casting process.
- The Cu core and mold are considered as rigid body.

Based on these assumptions, the mass, momentum, and energy conservations can be expressed as follows:

$$\text{Mass conservation} \quad \nabla \cdot \bar{V} = 0 \quad [1]$$

$$\begin{aligned} \text{Momentum conservation} \quad & \frac{\partial(\rho \bar{V})}{\partial t} + \nabla \cdot (\rho \bar{V} \bar{V}) \\ & = \nabla \cdot \left((\mu_t + \mu_l) \nabla \bar{V} \right) \\ & \quad - \nabla p - \frac{\mu_l}{K + \chi} (\bar{V} - \bar{V}_s) \\ & \quad + \rho \bar{g} \beta (T - T_{\text{coh}}) \end{aligned} \quad [2]$$

$$\begin{aligned} \text{Energy conservation} \quad & \frac{\partial(\rho H)}{\partial t} + \nabla \cdot (\rho \bar{V} H) \\ & = \nabla \cdot (\lambda \nabla T). \end{aligned} \quad [3]$$

The permeability in the two-phase region is calculated using the Kozeny–Carman equation:^[18]

$$K = \frac{K_0(1 - f_s)^3}{f_s^2}. \quad [4]$$

In the solid phase ($f_s = 1$), a very small positive number is used in the secondary source term (Darcy term) to avoid divergence of the conservation equation, while in the liquid phase and the early state of solidification, before the Al-Si eutectic reaction, a very large positive number is used to replace K to avoid singularity of Darcy term. As stated by Zhang *et al.*,^[19] Darcy flow becomes significant when the dendrite coherence occurs and a rigid dendrite skeleton is established.

Fluid flow in the liquid pool is generated by the thermally induced buoyancy forces and forced convection through the feeding launder (as shown in Figure 2). Turbulence may be generated when molten metal flows through the feeding launder into the liquid pool. The

damping of turbulence down into the liquid pool is a process that is hard to predict. Low-Reynolds number k - ε model, originally given by Launder and Spalding,^[20] is adopted for application in the whole domain and to account for the solidification phase change. The damping of turbulence in the mushy region is achieved using a Darcian term in this model.^[4] The governing equations for k and ε can be written as follows:

$$\begin{aligned} \text{Turbulent kinetic energy} \quad & \frac{\partial(\rho k)}{\partial t} + \nabla \cdot (\rho \bar{V} k) \\ & = \nabla \cdot \left[\left(\mu_t + \frac{\mu_l}{\sigma_k} \right) \nabla k \right] \\ & \quad + G_k - \rho \varepsilon - \frac{\mu_l}{K + \chi} k \end{aligned} \quad [5]$$

$$\begin{aligned} \text{Turbulent dissipation rate} \quad & \frac{\partial(\rho \varepsilon)}{\partial t} + \nabla \cdot (\rho \bar{V} \varepsilon) \\ & = \nabla \cdot \left[\left(\mu_t + \frac{\mu_l}{\sigma_\varepsilon} \right) \nabla \varepsilon \right] \\ & \quad + C_1 \frac{\varepsilon}{k} G_k - C_2 \rho \frac{\varepsilon^2}{k} \\ & \quad - \frac{\mu_l}{K + \chi} \varepsilon. \end{aligned} \quad [6]$$

In order to calculate the thermal contraction of solid shell and the air gap size, a linear thermoelastic model is needed to couple with the thermofluid model for the heat and melt flow. The stress equation can be written as follows:

$$[L]^T \{\sigma\} = 0. \quad [7]$$

In this thermoelastic model, the effect of thermal strain is taken into account. The strain–stress constitutive equation can be described by the Hooke's law:

$$\{\varepsilon\} = [D]_e^{-1} \{\sigma\} + \{\alpha(T) \Delta T\}. \quad [8]$$

In this study, the thermal expansion coefficient of solid phase $\alpha(T)$ is based on the coherency temperature T_{coh} and a function that depends upon temperature. The temperature range ΔT is the difference between the current temperature T and the coherency temperature T_{coh} .

B. Boundary Conditions

Different boundary conditions are applied to boundaries Γ of the computational domain (shown in Figure 2). At the melt flow inlet boundary Γ_1 , the temperature is prescribed equal to the casting temperature. The velocity is assumed to be uniform and calculated based on the inlet–outlet mass balance. At the top surface Γ_2 , hot-top boundary Γ_3 , and symmetry plane Γ_4 , the heat flux is assumed to be zero. At the outlet boundary Γ_5 , the bottom surface of hollow billet, the temperature is

constant at 300 K (27 °C) and the velocity is prescribed equal to the casting speed.

The thermal boundary conditions at the outer and inner walls of hollow billet are treated as Cauchy-type boundary conditions, which involves the prescription of HTC and external temperature. These thermal boundary conditions are prescribed in the following sections.

1. *Boundary conditions for the inner primary cooling zone Γ_6 and outer primary cooling zone Γ_7*

Figure 3 schematically shows the primary cooling region at the interface between the Cu core and hollow billet. The total height of this region is 120 mm (equal to the actual height of Cu core). This region can be divided into the upper contact zone and lower air gap zone. The same is true for the interface between the mold and hollow billet.

In the contact zone, the molten metal or soft mushy metal comes in contact with the core/mold. The interface shape is simplified as vertical because the shrinkage and deformation of the metal are compatible with the interface shape. The typical values of HTC in the contact zone range from 1000 to 5000 W/(m²K), while when the air gap forms, the values range from 100 to 500 W/(m²K).^[21–23] As observed by Ho and Pehlke,^[7] the HTC has a trend toward decrease with the increase of solid fraction even before the air gap forms. The HTC is assumed to vary linearly with the solid fraction using the following equation:

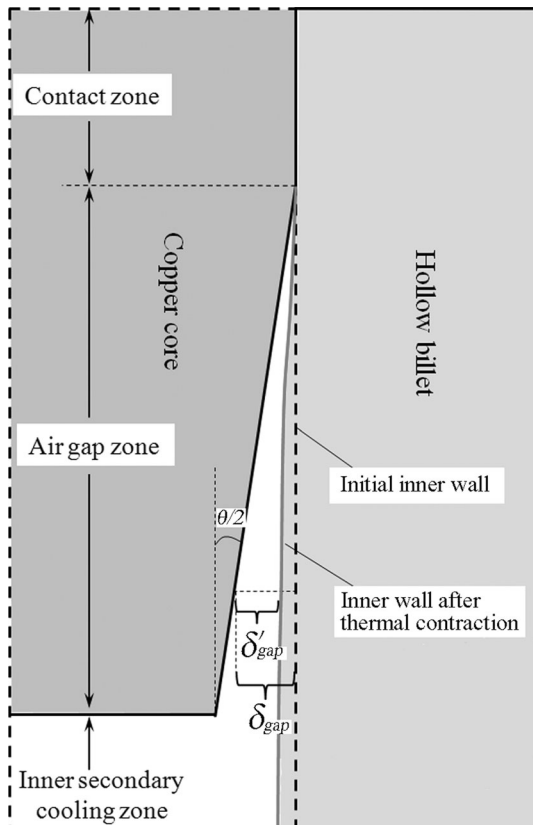


Fig. 3—Primary cooling region at the interface between core and hollow billet.

$$h = h_{\text{contact}} \times (1 - f_s) + h_{\text{air}} \times f_s, \quad [9]$$

where h_{contact} and h_{air} are the HTCs for the interface between hollow billet and core/mold in conforming contact and nonconforming contact conditions, respectively. The surrounding environment temperature is assumed to be 400 K (127 °C).

When the molten metal cools down and reaches the coherency temperature, the mushy metal starts to behave as a solid and thermal contraction of this solid shell begins to occur. When the thermal contraction occurs in the radial direction, the macroscopic air gap would form at both the inner and the outer walls of hollow billet. It can be clearly seen in Figure 3 that air gap width δ_{gap} decreases when the thermal contraction of hollow billet is considered. As suggested by Huang *et al.*,^[12] the HTC in the air gap zone can be calculated using the following equation:

$$h = \frac{\lambda_{\text{air}}}{A + B\delta_{\text{gap}}}, \quad [10]$$

where λ_{air} is the thermal conductivity of air, which is assumed to be 0.03 W/(mK). A is the roughness of the interface, which is assumed to be 1.06×10^{-5} m, and B is assumed to be 0.09 here. The surrounding air temperature is assumed to be 400 K (127 °C).

By calculating the thermoelastic strain field, the deformed shape of hollow billet can be obtained. Then the air gap width can be derived using the following formula:

$$\delta_{\text{gap}} = \sqrt{x_1^2 + y_1^2} - \left[r_{\text{core}} - (|z_1| - H_{\text{contact}}) \times \tan \frac{\theta}{2} \right], \quad [11]$$

where (x_1, y_1, z_1) are the coordinates of arbitrary point within the air gap zone at the inner wall of hollow billet, r_{core} is the radius of the outer wall of Cu core at the coordinates of (x_1, y_1, z_1) , H_{contact} is the height of contact zone, which is unknown beforehand and should be acquired by solving the coupled models of fluid flow and thermal contraction of solid shell, and θ is the Cu core taper angle.

As studied experimentally by Trovant and Argyropoulos,^[9] the HTC almost remains at the same value when the air gap width is larger than the certain value. In this study, the HTC is kept at a constant value of 300 W/(m²K) when the air gap width is larger than 1 mm. According to Eq. [10], the HTC as a function of air gap width at the air gap zone is shown in Figure 4.

2. *Boundary conditions for the inner secondary cooling zone Γ_8 and the outer secondary cooling zone Γ_9*

The HTC at the inner secondary cooling zone is assumed to be constant at 300 W/(m²K) because the inner wall of hollow billet is merely cooled by the surrounding air. The surrounding air temperature is assumed to be 300 K (27 °C).

The outer surface of hollow billet is cooled by cooling water. The corresponding boundary condition can be divided into two zones: the upper impingement zone and

the lower streaming zone. The values of HTC, as determined by Wells and Cockcroft,^[24] as the functions of wall surface temperature, water temperature, and water flow rate are shown in Figure 5. The cooling water temperature is 300 K (27 °C).

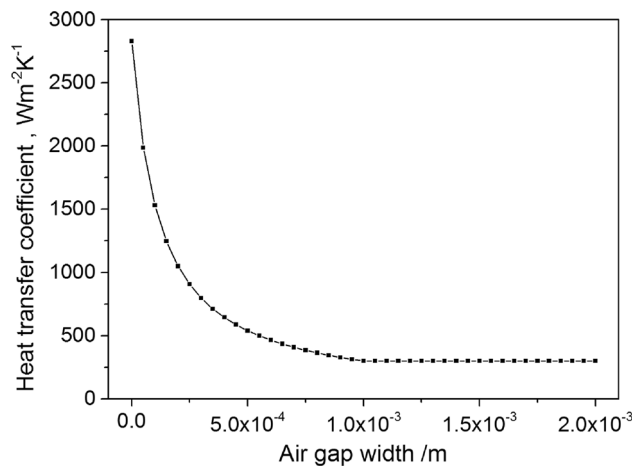


Fig. 4—HTC as a function of air gap width at air gap zone.

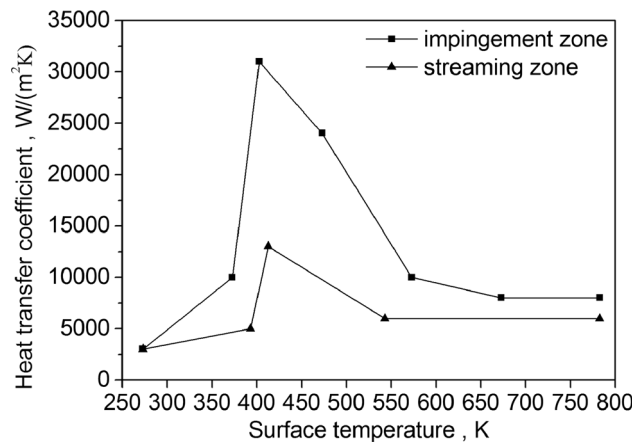


Fig. 5—HTC as a function of surface temperature of hollow billet in the outer secondary cooling zone.

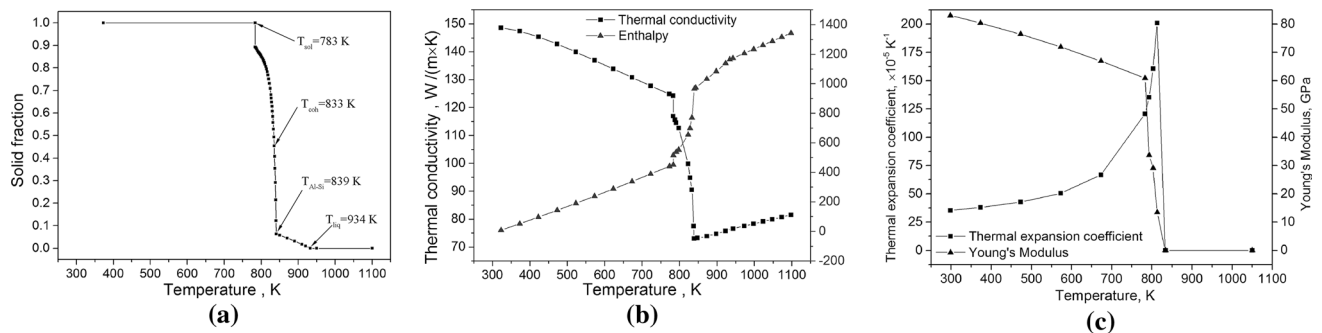


Fig. 6—Temperature-dependent physical properties in A390 alloy: (a) solid fraction, (b) thermal conductivity and enthalpy, and (c) thermal expansion coefficient and Young's modulus.

3. Boundary conditions for the calculation of thermal contraction

When the thermal contraction is to be calculated, an extra core mesh model must be inserted into the center of hollow billet because the free thermal contraction of the inner wall is constrained by the Cu core. The interface between the outer wall of Cu core and the inner wall of hollow billet is set as the contact pair. The displacement at the symmetry plane is set to be 0. The displacement at the isotherm of coherency temperature where the thermal contraction starts should also be set to 0, because the coherency temperature is a temperature at which the alloy in the mushy zone begins to behave as a linear elastic solid. Unfortunately, this isotherm is not always right on the nodes. It is simplified by setting the displacement constraint at the melt level and ignoring the liquid shrinkage, because the melt level is constant due to the continuous supply of melt into the cavity during the DC casting process.

C. Material Data

In this study, the commercial software JMatPro was used to calculate the physical properties of A390 alloy. Figure 6 shows the temperature-dependent solid fraction, thermal conductivity, enthalpy, thermal expansion coefficient, and Young's modulus of A390 alloy. As shown in Figure 6(a), the solid fraction increases slowly at first corresponding to the formation of primary Si particles in the molten metal, and then it increases rapidly to the solidus temperature of 783 K (510 °C) after the temperature reached the eutectic temperature of 839 K (566 °C). The coherency temperature is assumed to be reached when the temperature is 833 K (560 °C). The constant physical properties of A390 alloy are listed in Table I.

D. Numerical Implementation

The commercial software FLUENT was used to simulate the melt flow, heat transfer, and solidification in the hollow billet. User-defined functions (UDFs) were written in FLUENT for the momentum source terms and boundary conditions. The Abid low-Reynolds number turbulence model was used.^[25] The SIMPLE algorithm was used for velocity–pressure coupling. The

under-relaxation factor of pressure is 0.1, momentum, turbulent kinetic energy, and turbulent dissipation rate is 0.2, density and body forces is 0.3, and turbulent viscosity and energy is 0.5. The PREstressed Option (PRESTO) scheme was used for pressure correction equations. The first-order upwind scheme was used to discretize the momentum, turbulent kinetic energy, and turbulent dissipation rate equations, and second-order upwind scheme was used to discretize the energy equation.

The commercial software ANSYS was used to simulate the thermal contraction in the hollow billet. The temperature distribution (each iteration except for the

initial uniform temperature distribution) was computed by FLUENT software.

Figure 7 schematically shows the flow chart of simulation procedure to solve the coupled model. During the operation, H_{total}^i represents the total height of the hollow billet at the iteration number i . The iteration number i is increased until $|H_{total}^i - H_{total}^{i-1}| < \delta$ (δ is a small and finite error), considering that the demanded condition is implemented, and the computing process moves to the next step. H_0 represents the initial height of contact zone at the inner wall, which is initially a small value. H'_0 represents the calculated height of contact zone. When the calculated value of H'_0 is larger than the initial value, which means that the initial value of H_0 should be increased until the two values coincide well. Only then the calculated value of H'_0 can be considered as the theoretical height of contact zone at the inner wall.

For example, assume that the core taper angle is 3 deg, the casting speed is 1.83 mm/s, and the casting temperature is 1050 K (777 °C). The melt contact region at the side wall of the Cu core is unknown at the beginning. The initial height of contact region (H_0) is set to a small initial value of 10 mm. The temperature distribution in the hollow billet is calculated by FLUENT software and then the thermal contraction of the geometrical model is simulated by ANSYS software. Figure 8(a) shows the temperature distribution of the hollow billet with deformed geometry after three iterations of the coupled simulation process. The height between the top edge of mold and position of the initial solid shell at the inner wall is 40 mm (defined as H'_0 hereafter), which is much larger than H_0 (10 mm). The molten metal below the contact region (in the region range of H_0 to H'_0) would leak out from the inner surface into the air gap. It is obvious that the initial contact region at the inner wall should be increased until the molten metal can be safely supported by the inner solid shell. Only when the initial height of contact region H_0 is set to 25 mm, as shown in the Figure 8(d), the numerical result of H'_0 is equal to H_0 . The predicted value of H'_0 (25 mm) is considered as the theoretical height of contact zone at the inner wall for the predefined casting parameters described above.

E. Grid Independency Test

The grid independency tests were carried out using five different grid resolutions (presented in radial, circumferential, and axial directions), as listed in Table II. Figure 9 shows the sump shapes at the symmetry plane for all grid settings. It is obvious that the boundary layers at the inner and the outer wall are necessary to simulate temperature distribution at the inner and outer walls accurately. The variation in sump shape is relatively small when the uniform grid size is smaller than 10 mm in the axial direction (case 3 and case 4 in Table II). For the purpose of reducing computational time, nonuniform grids were used as shown in Table II (case 5). When comparing the results of case 3 and case 4, an acceptable accuracy of sump

Table I. Constant Physical Properties of A390 Alloy

Density, ρ	2600 kg/m ³
Liquidus, T_l	934 K (661 °C)
Al-Si eutectic reaction temperature	839 K (566 °C)
Solidus, T_s	783 K (510 °C)
Viscosity, μ_l	0.0015 Pa s
Volume expansivity, β	$4.29 \times 10^{-5}/K$
Reference temperature, T_0	833 K (560 °C)
Initial permeability, K_0	$1 \times 10^{-10} m^2$
Poisson's ratio, ν	0.33

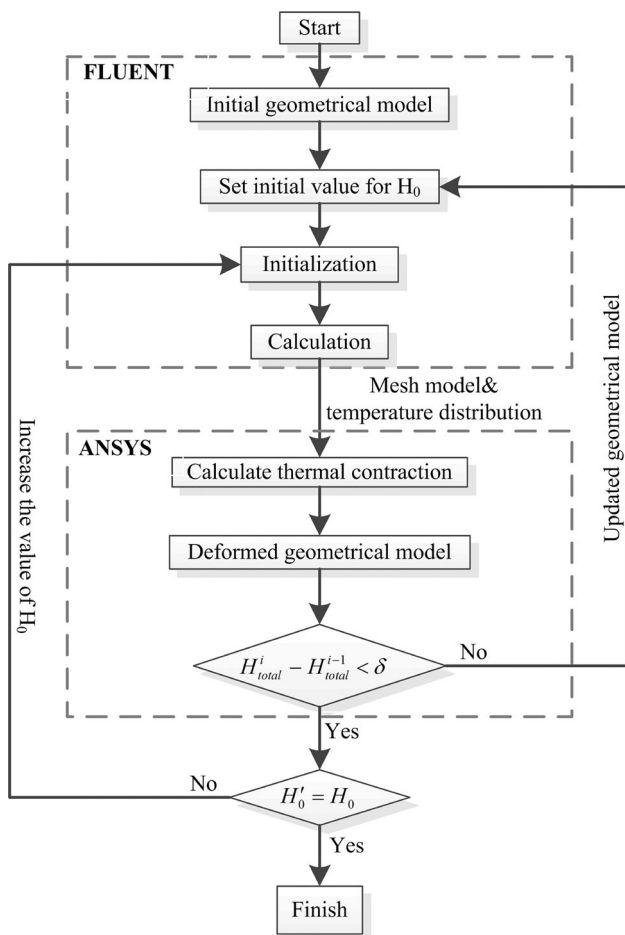


Fig. 7—Programmatic flow chart of the calculation of coupled mathematical model.

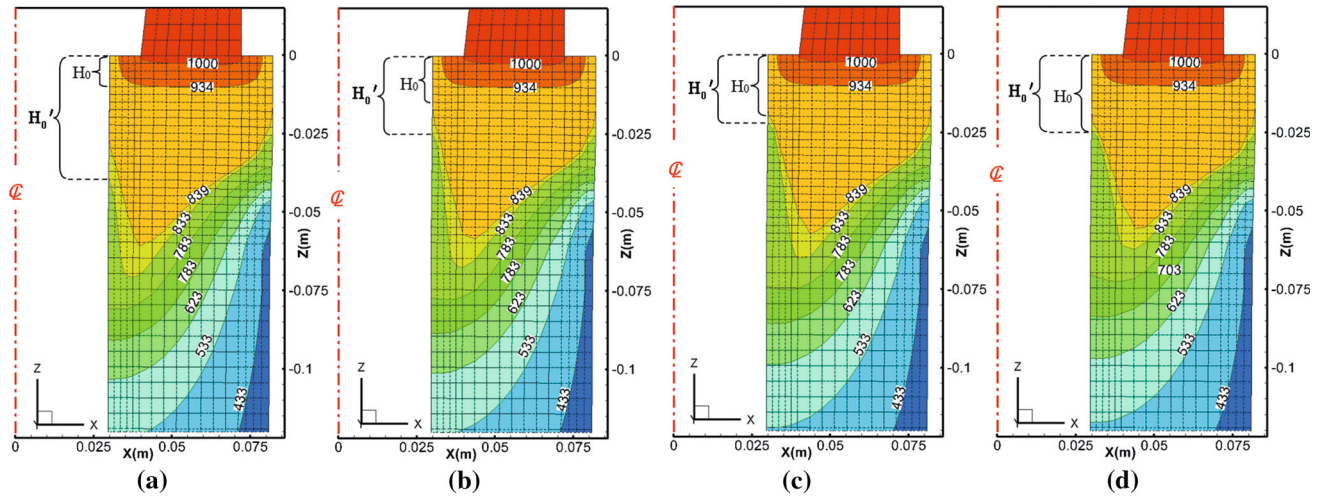


Fig. 8—Effect of initial contact height at the inner wall on the temperature profile of hollow billet during DC casting: (a) 10 mm, (b) 15 mm, (c) 20 mm, and (d) 25 mm.

Table II. Grid Parameters for Mesh Independence Test

Cases	Grid Size $r \times \phi \times z$ (mm)	Total Number	Boundary Layer	Remarks
1	$5 \times 5 \times 5$	190,660	no	—
2	$5 \times 5 \times 10$	141,100	yes	thickness of boundary layer at the inner and outer walls is 10 mm (grid size of 2 mm in the radial direction)
3	$5 \times 5 \times 5$	282,660	yes	—
4	$5 \times 5 \times 2.5$	305,880	yes	when $z < -120$ mm, grid size at z -direction is 5 mm.
5	$5 \times 5 \times z$ (simplified)	129,460	yes	when $z < -300$ mm, grid size at z -direction is 20 mm; when $-60 \text{ mm} \leq z \leq 0$ mm, grid size at z -direction is 2.5 mm; else grid size at z -direction is 5 mm

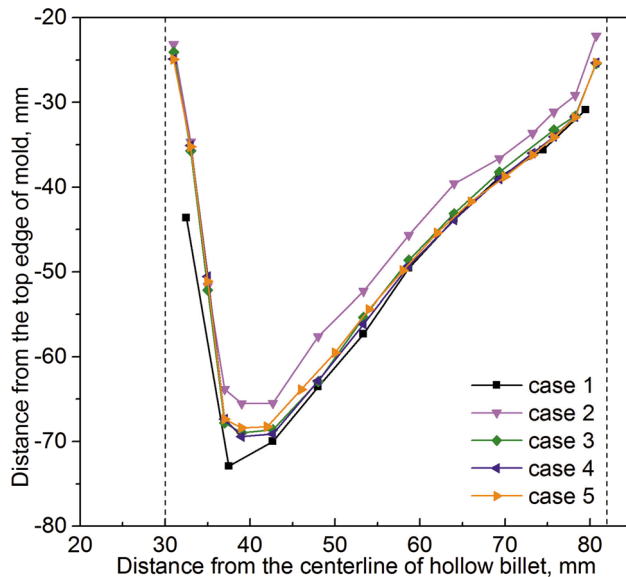


Fig. 9—Comparison of sump shape under different mesh sizes.

shape can be obtained with these nonuniform grids. Therefore, all simulation works reported in this paper were carried out with nonuniform grid distribution as shown in Table II.

F. Model Validation

Figure 10 shows the comparison of the simulation and experimental results of cooling curves and an outline of the hollow billet. The casting parameters are as follows: the core taper angle is 3 deg, the casting speed is 1.83 mm/s, and the casting temperature is 1050 K (777 °C). As shown in Figure 10(a), there is a good agreement between the simulated and measured cooling curves. As shown in Figure 10(b), the simulated diameter of the outer wall (160.9 mm) almost coincides with that of the cast hollow billet (160.8 to 161.2 mm). The actual diameter of the inner wall (57.0 to 57.4 mm) is somehow smaller than the numerical value (58.8 mm). This can be attributed to the fact that the inner wall is partially remelted and exudation of liquid metal forms after air gap generation. It can be seen that the coupled

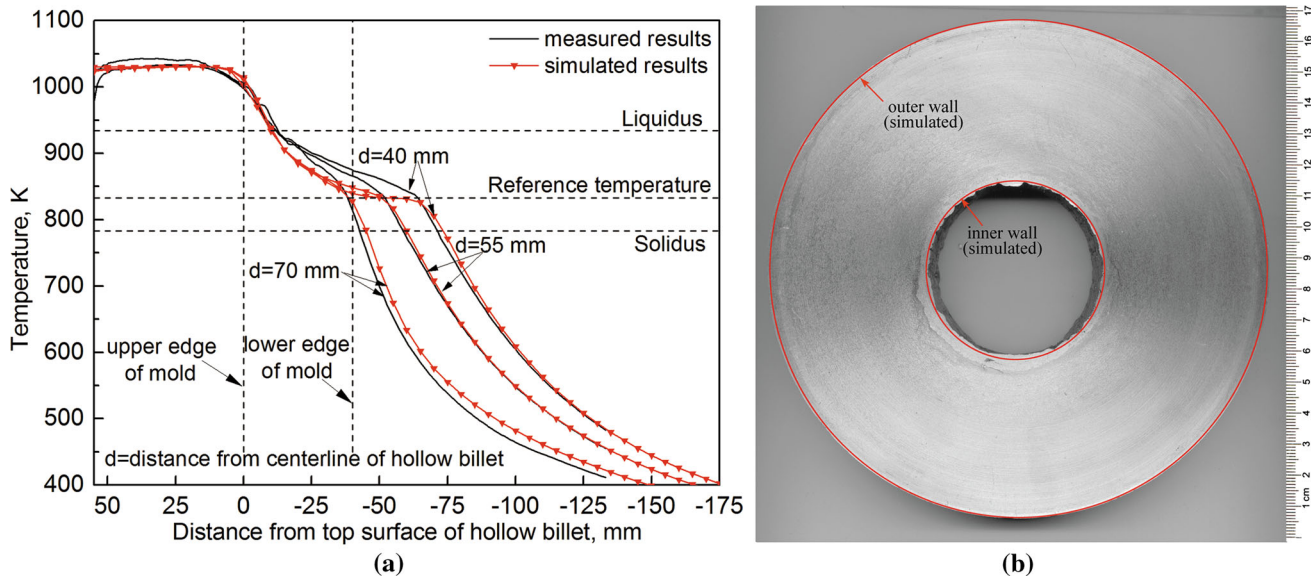


Fig. 10—Comparison between the simulated and measured results of (a) cooling curves and (b) outer and inner wall diameters.

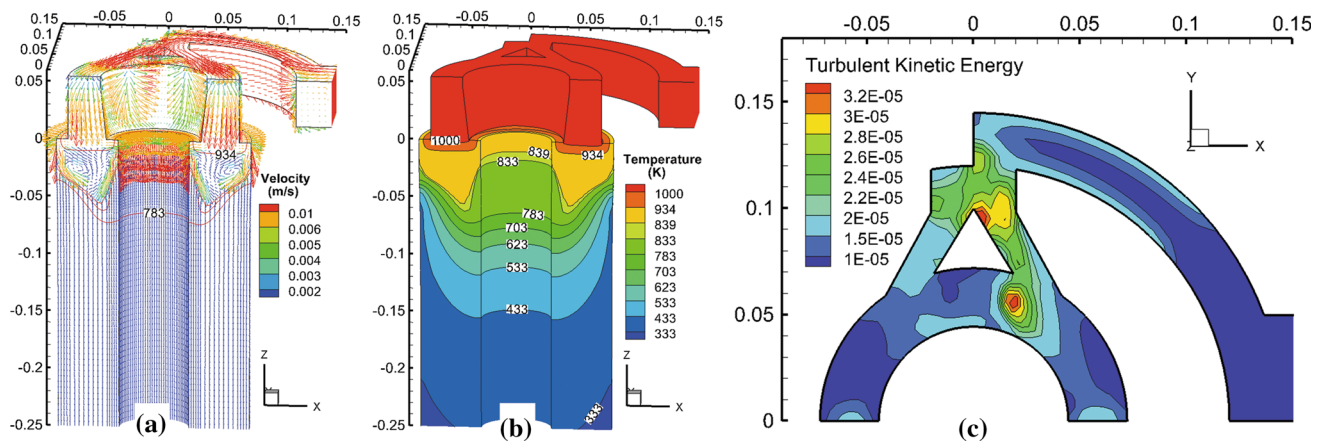


Fig. 11—(a) Velocity vector field, (b) temperature field, and (c) turbulent kinetic energy in the A390 alloy hollow billet cast at 1.83 mm/s and 1050 K (777 °C) with the core taper angle of 3 deg.

mathematical model developed in this paper is able to predict the temperature distribution and thermal contraction of the hollow billet during DC casting process.

III. RESULTS AND DISCUSSION

In this section, the simulated results of the DC casting process for hollow billet based on the coupled mathematical model are presented.

To begin with, the simulated results are presented in a typical case with the core taper angle of 3 deg, casting speed of 1.83 mm/s, and the casting temperature of 1050 K (777 °C). Figure 11 shows the velocity vector field, temperature field, and turbulent kinetic energy in the A390 alloy hollow billet. As shown in Figure 11(a), it can be seen that the molten metal is fed horizontally into the cavity surrounded by the inner and outer hot tops and then its direction gradually deflects downward.

After the melt reaches the upper edge of the mold/Cu core, it flows downward along the side wall of the mold/Cu core, solid front, and then solidifies into the hollow billet. The velocity at the solid front is somewhat larger than that in the interior zone.

It is obvious that the molten metal is maintained at high temperature with its position being higher than the upper edge of the mold, as shown in Figure 11(b). When the molten metal contacts with the mold/Cu core, the melt temperature declines quickly to below the liquidus and solid shell forms at both the outer and the inner walls. When the solid shell is pulled out from the mold, the temperature decreases sharply because the secondary cooling water impinges directly onto the outer wall. The temperature of the inner solid shell remains in the range between the solidus and coherency temperatures for a rather long distance owing to the low heat dissipation rate at the inner wall. As a result, the bottom of each isotherm gradually moves toward the inner wall of the

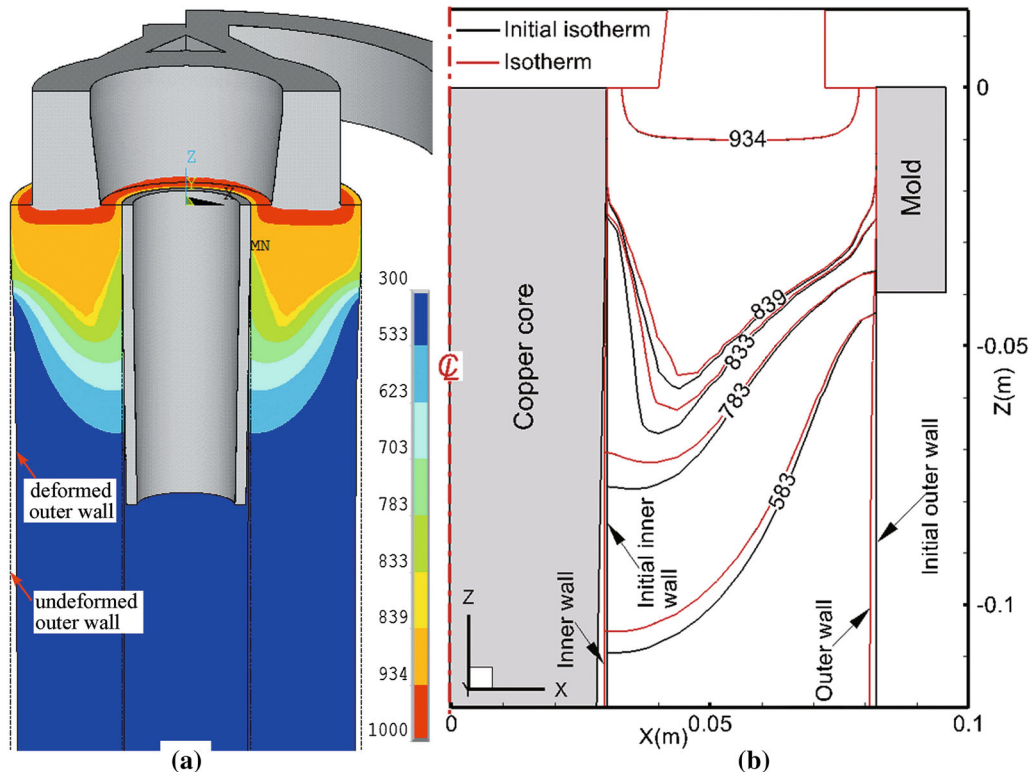


Fig. 12—Effect of thermal contraction of hollow billet on the (a) geometry shape and (b) temperature profiles at the symmetry plane.

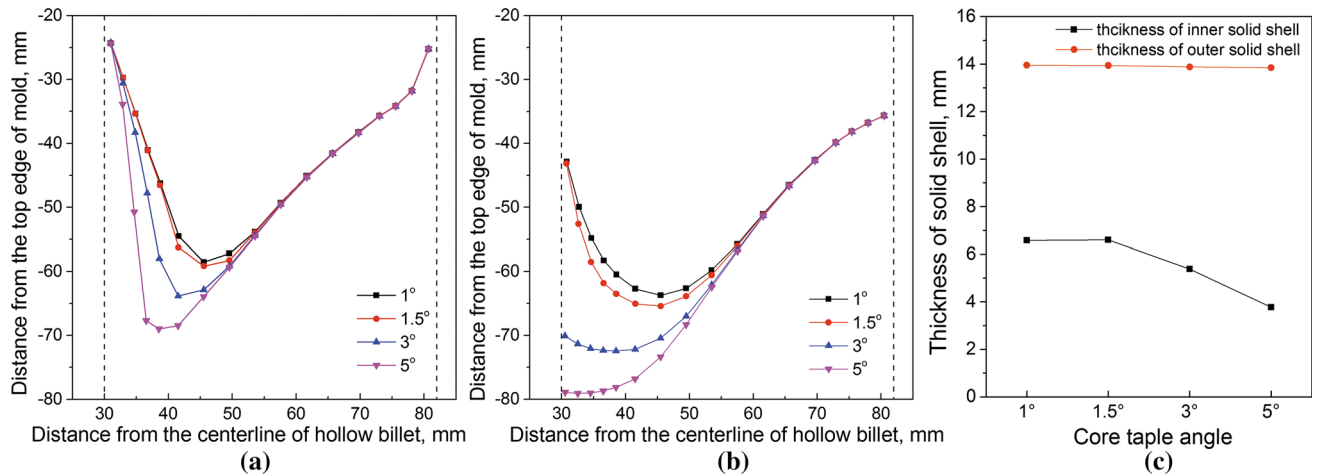


Fig. 13—Isotherms at the symmetry plane under different core taper angles: (a) coherency temperature, (b) solidus, and (c) thickness of solid shell.

hollow billet. It can clearly be seen from Figure 11(c) that turbulence plays an important role in the transport process, especially at the top region of liquid pool.

The investigation of temperature profiles will be carried out only on the right side of $z-x$ symmetry plane hereafter. Because the temperature profiles at each longitudinal section across the centerline are almost the same. Figure 12 shows the geometry shape and temperature profile at the symmetry plane before and after taking the thermal contraction of hollow billet into account. It can be clearly seen that both the inner and

the outer walls shrink after the calculation of thermal contraction. What is more, each isotherm climbs in the hollow billet, especially in the inner half part of the hollow billet. This can be attributed to the fact that the shrunk inner wall decreases the air gap width while increasing the HTC between the hollow billet and Cu core. Therefore, more heat is extracted through the inner wall of the hollow billet. However, the formation position of the initial solid shell at the inner wall remains unchanged because it is mainly affected by the molten metal flow.

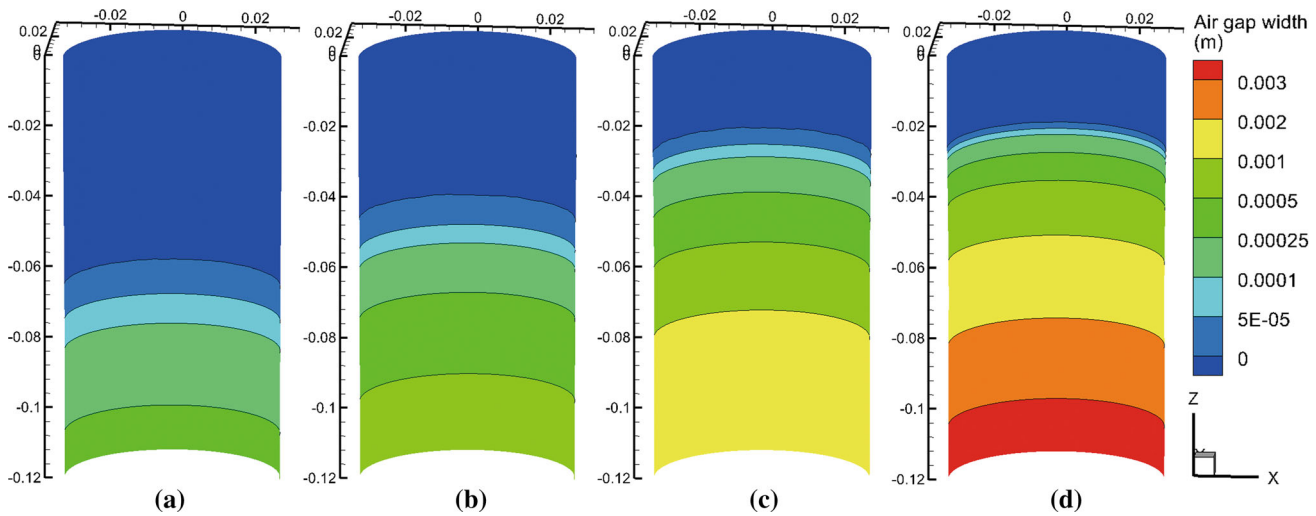


Fig. 14—Air gap width mapped onto the inner wall of hollow billet under different core taper angles: (a) 1 deg, (b) 1.5 deg, (c) 3 deg, and (d) 5 deg.

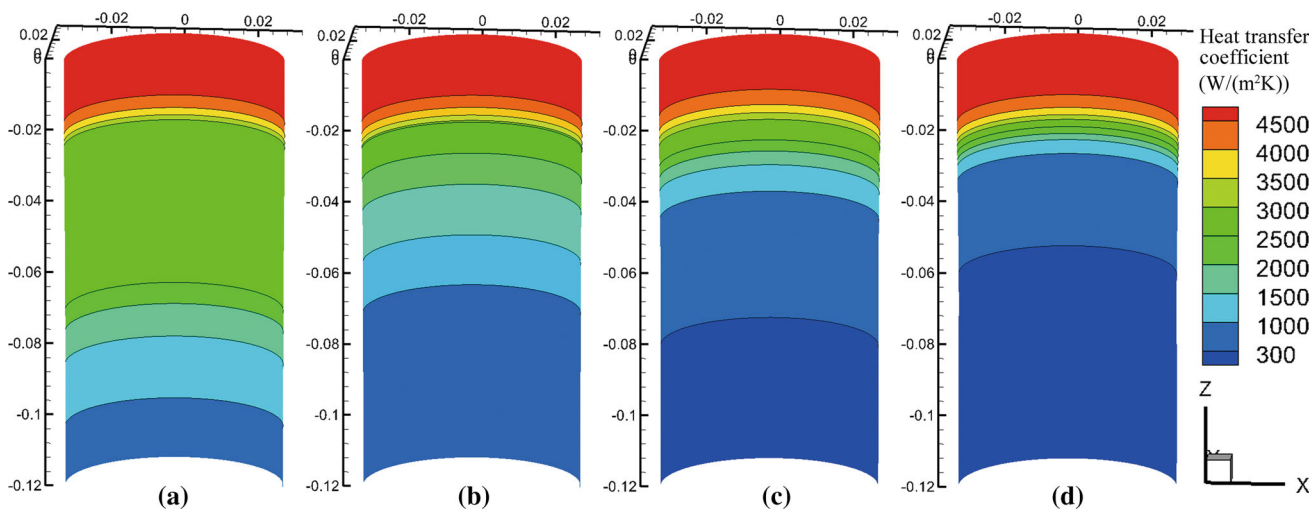


Fig. 15—Heat transfer coefficient mapped onto the inner wall of hollow billet under different core taper angles: (a) 1 deg, (b) 1.5 deg, (c) 3 deg, and (d) 5 deg.

A. Effect of Core Taper Angle

Figure 13 shows the variation of sump shape, solidus isotherm, and thickness of solid shell (exit of mold) in the hollow billet at the symmetry plane as a function of core taper angle in the range of 1 to 5 deg, the casting speed of 1.83 mm/s, and the casting temperature of 1050 K (777 °C). It is clearly shown in Figure 13 that the isotherms of coherency temperature and solidus and solid shell thickness are significantly affected at the inner half part while remaining almost unchanged at the outer half part of the hollow billet by the variation of core taper angle. With the increase of core taper angle, the sump depth increases, the solid shell thickness becomes thinner, and the solidus isotherm moves downward. However, the formation position of the initial solid shell at both the inner and outer walls is constant at 25 mm

below the upper edge of the mold. The reason is that the formation position is affected primarily by the molten metal flow.

As shown in Figures 13(a) and (b), at the core taper angles of 1, 1.5, 3, and 5 deg, the bottom of the sump shape is 58.6, 59.2, 63.8 and 69.0 mm, while that of the solidus isotherm at the inner wall is 42.9, 43.1, 70.1 and 78.9 mm below the upper edge of mold, respectively. The differences can be well understood by examining the air gap width δ_{gap} and HTC at the inner wall of the hollow billet. Figure 14 schematically shows the contour plot of δ_{gap} mapped onto the inner wall of the hollow billet under different core taper angles. It can be clearly seen that δ_{gap} increases significantly but the height of $\delta_{\text{gap}} = 0$ zone decreases with the increasing core taper angle. Figure 15 schematically shows the contour plot of

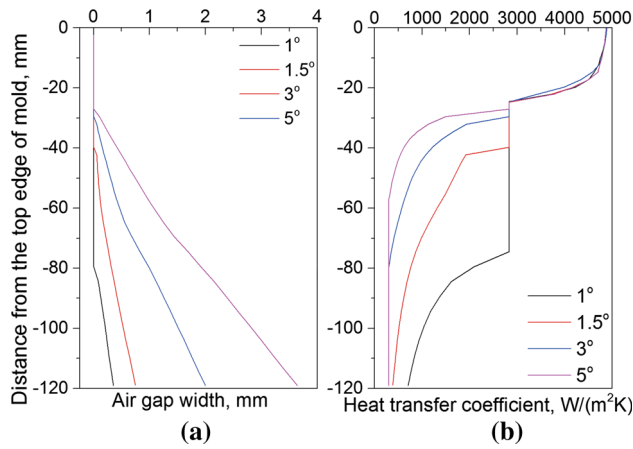


Fig. 16—(a) Air gap size δ_{gap} and (b) HTC on the symmetry plane at the inner wall as a function of distance from the upper edge of mold under different core taper angles.

HTC mapped onto the inner wall of the hollow billet. It can be seen that HTC decreases monotonically with the increasing distance from the upper edge of mold. A higher HTC can be obtained and more heat quantity can be extracted at the inner wall by decreasing the core taper angle, which in turn causes the isotherms move upward in the hollow billet.

For the purpose of better demonstration of the effect of the core taper angle on the simulated results, Figure 16 shows the variation of δ_{gap} and HTC on the symmetry plane at the inner wall. It can be observed that, before the formation of solid shell at the inner wall, the air gap width is zero, while the value of HTC decreases with increasing the distance from the upper edge of mold. However, no obvious difference in HTC is found with the variation of core taper angle. It can be inferred that the temperature evolution is almost identical at the inner wall. After the solid shell formed at the inner wall, the HTC in the $\delta_{\text{gap}} = 0$ zone remains constant at 2830 W/(m²K) and then decreases with the increase of air gap width. The value of HTC decreases with the increase of core taper angle at each distance from the upper edge of mold. When the air gap width is larger than 1 mm, the HTC remains constant at 300 W/(m²K) as assumed.

As shown in Figure 16(a), the real height of contact zone ($\delta_{\text{gap}} = 0$) is 79.5, 39.7, 29.5, and 27.1 mm at the core taper angles of 1, 1.5, 3, and 5 deg, respectively, which are larger than the theoretical values of contact height (25 mm). The reason is that the thermal contraction of solid shell eliminates the air gap just beneath the formation position of the initial solid shell at the inner wall. The surface temperature of the inner wall corresponding to the position where hollow billet detaches from the core is 637 K, 789 K, 816 K, and 826 K (364 °C, 516 °C, 543 °C, and 543 °C) at the core taper angles of 1, 1.5, 3, and 5 deg, respectively. It can be seen that the Cu core still remains in contact with the inner wall even if the inner wall is totally solidified when the core taper angle is 1 deg. There is no doubt that high contact pressure, which originates from the shrinkage of

the initial solid wall, would prevent the separation of the hollow billet from the core and cause the “hanging” problem. The detaching position lies in the semi-solid region at the core taper angles of 1.5, 3, and 5 deg. The research on the tensile strength of semi-solid multi-component aluminum alloys shows that the strength increases slowly with the decreasing temperature until several degrees above the solidus.^[26] It can be inferred that the “hanging” problem is likely to happen during the DC casting process using the core taper angle of 1.5 deg. Because the temperature of the detaching position at the inner wall is just 6 deg above the solidus, the strength of the inner solid shell and the contact pressure are relatively high and might prevent the separation of the hollow billet from the Cu core. However, no threat of “hanging” problem would occur when using the core taper angles of 3 and 5 deg, because the strength of the inner solid shell and the contact pressure are relatively low as the temperature is rather high in the mushy zone. It can be concluded that the temperature of the detaching position at the inner wall can be considered as the criterion to determine the possibility of successful casting of hollow billet. Although the breakout of molten metal can be prevented by the solid shell, low-melting point Al-Si-Cu eutectic would penetrate the inner wall and make the inner wall rough during the DC casting process. It is suggested that the optimal core taper angle is set to 3 deg to prevent the inner wall from becoming rougher at higher core taper angle.

B. Effect of Relative Vertical Position of Core in the Mold

By adjusting the vertical position of Cu core in the mold, the effect of relative position difference between the core and the mold on the simulated results is presented in this section. The value of relative position difference represents the difference of vertical position between the upper edge of the core and the mold. Figure 17 shows the sump shape, solidus isotherm, and solid shell thickness (exit of mold) on the symmetry plane under different relative position differences with setting the core taper angle constant at 3 deg. As shown in Figures 17(a) and (b), with lowering the vertical position of Cu core, the sump shape, solidus isotherm, and the formation position of the initial solid shell at the outer wall move downward. However, the formation position of the initial solid shell at the inner wall is almost unaffected (about 25 mm below the upper edge of the mold). The solid shell thickness becomes deeper at both the outer and inner walls. This can be related to the fact that the flow velocity of molten metal has changed, as shown in Figure 18. With lowering the vertical position of Cu core, the flow of molten metal impacts on the outer wall of Cu core is depressed, while that on the inner wall of the mold is encouraged. The residence time of hot molten metal in the mold decreases with the increasing flow rate of molten metal, which in turn delays the formation of the initial solid shell. In contrast, the depressed melt flow causes the decrease of contact height between the molten metal and the Cu core significantly.

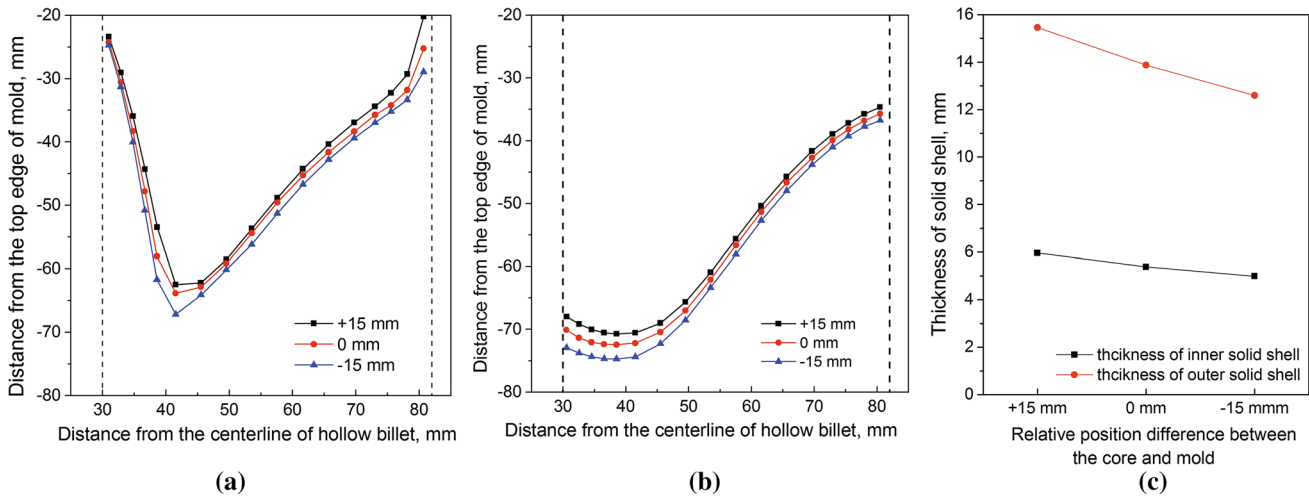


Fig. 17—(a) Sump shape, (b) solidus isotherm, and (c) thickness of solid shell on the symmetry plane under different relative position differences.

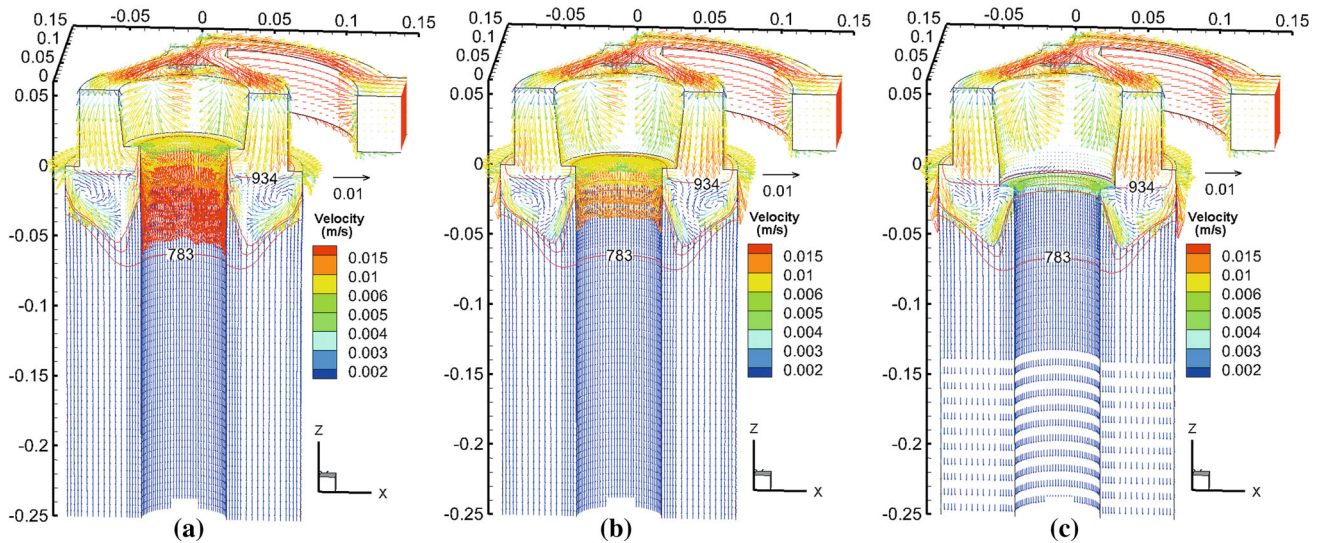


Fig. 18—Velocity vector in the A390 alloy hollow billet under different relative position differences at the core taper angle of 3 deg: (a) +15 mm, (b) 0 mm, and (c) -15 mm.

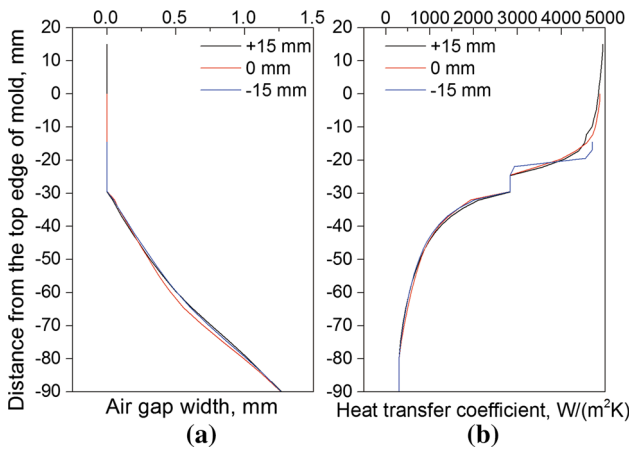


Fig. 19—(a) Air gap size δ_{gap} and (b) HTC on the symmetry plane at the inner wall as a function of distance from the upper edge of mold under different relative position differences.

Figure 19 shows the variation of δ_{gap} and HTC on the symmetry plane at the inner wall under different relative position differences. Each value of δ_{gap} and HTC is almost identical as a function of distance from the upper edge of the mold under all conditions of relative position difference. It can be seen that, with the relative position difference values of 15, 0, and -15 mm, the real contact height between the core and the hollow billet is 44.6, 29.5, and 15 mm, respectively, which are larger than the corresponding theoretical contact height values of 40, 25, and 10 mm. However, the hollow billet can be successfully prepared regardless of the variation in the relative height between the core and the mold. The main reason is that the temperature of the detaching position at the inner wall is in the range of 812 K to 817 K (539 °C to 544 °C). The strength of the solid shell in this temperature range is rather low, which in turn makes the contact pressure between the core and hollow billet

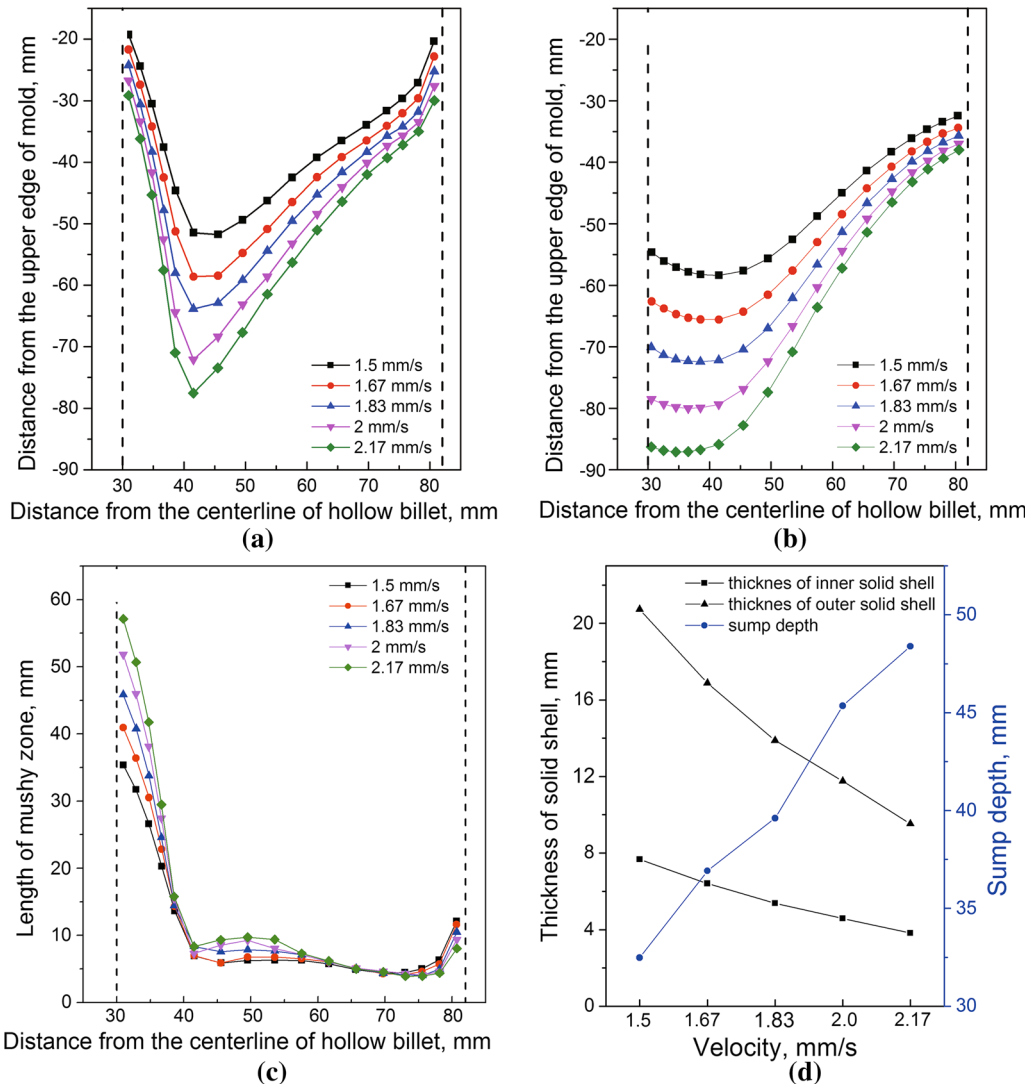


Fig. 20—(a) Sump shape, (b) solidus isotherm, (c) length of mushy zone, and (d) thickness of solid shell and sump depth on the symmetry plane under different casting speeds.

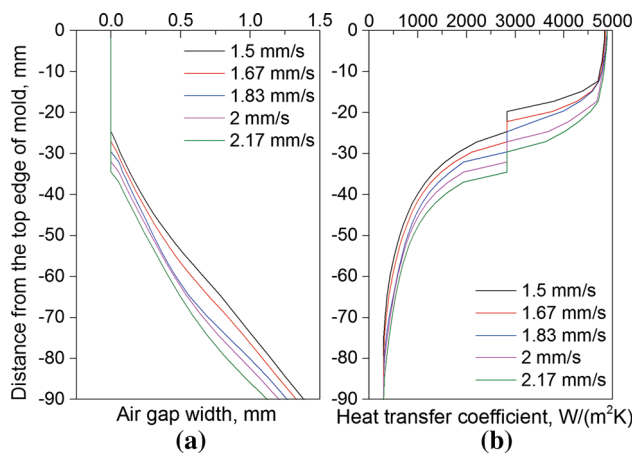


Fig. 21—(a) Air gap size δ_{gap} and (b) HTC on the symmetry plane at the inner wall as a function of distance from the upper edge of mold under different casting speeds.

very low. As a result, the hollow billet can detach easily from the core during the DC casting process.

C. Effect of Casting Speed

Figure 20 shows the sump shape, solidus isotherm, mushy zone length, solid shell thickness, and sump depth on the symmetry plane under different casting speeds with the core taper angle being constant at 3 deg. As shown in Figures 20(a) and (b), at the casting speeds of 1.5, 1.67, 1.83, 2, and 2.17 mm/s, the formation position of the initial solid shell at the inner wall is 20, 22.5, 25, 27.5, and 30 mm below the upper edge of the mold, respectively. It can be seen that the formation position of the initial solid shell and each isotherm move downward, the sump depth increases, and the solid shell thickness decreases with the increase of casting speed. The reason is that higher molten metal

flow rate and higher heat quantity feed into the cavity at higher casting speed.

The mushy zone length at the inner wall is much higher than that in the outer regions (Figure 20(c)) due to the rather low cooling intensity at the inner wall. However, the mushy zone length at the outer wall is slightly higher than that at the subsurface because the cooling intensity sharply increases when the secondary cooling stage begins. With the increase of casting speed, the mushy zone length increases at the inner wall but slightly decreases at the outer wall. Because the thinner thickness of the outer solid shell at the exit of mold suffers higher cooling intensity in the secondary cooling stage.

Figure 21 shows the variation of δ_{gap} and HTC on the symmetry plane at the inner wall under different casting speeds. As shown in Figure 21, the real contact height between the core and the hollow billet is 24.6, 27.1, 29.5, 32.0, and 34.5 mm at the casting speed ranging from 1.5 to 2.17 mm/s, respectively, which are larger than the corresponding theoretical values of contact height. However, the hollow billets can be successfully prepared over the range of casting speed explored here. Because the temperature of the detaching position at the inner wall is in the range of 814 K to 817 K (541 °C to 544 °C), the strength of the inner solid shell is very low. The hollow billet can separate easily from the core due to the very low contact pressure.

IV. CONCLUSIONS

In this study, a mathematical model for the simulation of DC casting process of hollow billet was developed. The current model is unique in that the effects of core taper angle, relative vertical position of core in mold, and contact height between the core and the hollow billet were modeled. The primary cooling between the core and the hollow billet was modeled by a 3-dimensional analysis of melt flow, heat transfer, and solidification with considering the thermal contraction of hollow billet. The use of this model led to the following conclusions:

1. Considering the thermal contraction of hollow billet, the diameters of both the inner and outer walls shrink and each isotherm moves upward in the hollow billet due to the decreased air gap width and enhanced heat transfer coefficient between the core and the hollow billet.
2. With the increase of core taper angle, the sump depth and air gap width increase, the inner solid shell thickness, heat transfer coefficient, and real contact height between the core and the mold decrease, which in turn cause the decrease of the contact pressure. The core taper angle should be larger than 1.5 deg to avoid the possibility of “hanging” problem during the DC casting process. The optimal core taper angle of 3 deg is obtained in this study.
3. With lowering the position of core, the sump shape slightly moves downward, the solid shell thickness at both the inner and outer walls decreases, the real

contact height between the core and the hollow billet decreases sharply, while the formation position of the initial solid shell and the air gap width are unaffected. The hollow billet can be cast successfully under all the relative position differences explored in this study.

4. With the increasing casting speed, the sump depth, mushy zone length, and the real contact height between the core and the mold increase, the air gap width decreases, and the sump shape and solid shell move downward. However, the hollow billet can be cast successfully under the casting speed of 1.5 to 2.17 mm/s.

ACKNOWLEDGMENTS

This work was supported by the National Natural Science Foundation of China (No. 51204046) and the Fundamental Research Funds for the Central Universities (No. N130409003).

NOMENCLATURE

A	A constant value
B	A constant value
C_1	A constant value
C_2	A constant value
$[D]_e$	Elastic stiffness matrix
f_s	Solid fraction
g	Gravitational acceleration
G_k	Generation of turbulent kinetic energy
H	Enthalpy
H_0	Initial contact height
H_{contact}	Contact height
H_{total}	Total height of hollow billet
h	Heat transfer coefficient
h_{contact}	Good thermal contact coefficient
h_{gap}	Poor thermal contact coefficient
i	Iteration number
K	Permeability
K_0	Initial permeability
k	Turbulent kinetic energy
L	Differential operator
P	Pressure
r_{core}	Radius of Cu core
T	Current temperature
T_{coh}	Reference temperature
T_1	Liquidus
T_s	Solidus
t	Time
V	Velocity
V_s	Casting speed
(x_1, y_1, z_1)	Coordinate at the inner wall
$\alpha(T)$	Thermal expansion coefficient
β	Volume expansion coefficient at temperature T_0
δ	Small positive number
δ_{air}	Air gap width

ΔT	Temperature difference
ε	Turbulent dissipation rate
$\{\varepsilon\}$	Total strain vector
θ	Core taper angle
λ	Thermal conductivity
λ_{air}	Thermal conductivity of air
μ_l	Laminar viscosity
μ_t	Turbulent viscosity
ν	Poisson's ratio
ρ	Density at temperature T_0
$\{\sigma\}$	stress vector
σ_k	Turbulent Prandtl numbers for k
σ_ε	Turbulent Prandtl numbers for ε
χ	Very small positive number

REFERENCES

1. D.G. Eskin: *Physical Metallurgy of Direct Chill Casting of Aluminum Alloys*, CRC Press, Boca Raton, 2008, pp. 1–18.
2. D.C. Weckman and P. Niessen: *Can. Metall. Q.*, 1984, vol. 23, pp. 209–16.
3. M.R. Aboutalebi, M. Hasan, and R.I.L. Guthrie: *Numer. Heat Transf. A*, 1995, vol. 28, pp. 279–97.
4. D. Mortensen: *Metall. Mater. Trans. B*, 1999, vol. 30B, pp. 119–33.
5. C.J. Vreeman, J.D. Schloz, and M.J.M. Krane: *Trans. ASME J. Heat Transf.*, 2002, vol. 124, pp. 947–53.
6. L. Begum and M. Hasan: *Numer. Heat Transf. A*, 2015, vol. 67, pp. 719–45.
7. K. Ho and R.D. Pehlke: *Metall. Trans. B*, 1985, vol. 16, pp. 585–94.
8. R.W. Lewis and R.S. Ransing: *Metall. Mater. Trans. B*, 1998, vol. 29B, pp. 437–48.
9. M. Trovant and S. Argyropoulos: *Metall. Mater. Trans. B*, 2000, vol. 31B, pp. 75–86.
10. A. Prasad and I. Bainbridge: *Metall. Mater. Trans. A*, 2013, vol. 44A, pp. 456–68.
11. J.P. Verwijs and D.C. Weckman: *Metall. Trans. B*, 1988, vol. 19, pp. 201–12.
12. H. Huang, V.K. Suri, J.L. Hill, and J.T. Berry: *J. Eng. Mater. Technol. Trans. ASME*, 1993, vol. 115, pp. 2–7.
13. P. Chow, C. Bailey, M. Cross, and K. Pericleous: in *Modelling of Casting, Welding and Advanced Solidification Processes VII*, London, TMS, Warrendale, PA, 1995, pp. 213–21.
14. A.R. Baserinia, H. Ng, D.C. Weckman, M.A. Wells, S. Barker, and M. Gallerneault: *Metall. Mater. Trans. B*, 2012, vol. 43B, pp. 887–901.
15. A.R. Baserinia, E.J.F.R. Caron, M.A. Wells, D.C. Weckman, S. Barker, and M. Gallerneault: *Metall. Mater. Trans. B*, 2013, vol. 44B, pp. 1017–29.
16. W.D. Bennon and F.P. Incropera: *Int. J. Heat Mass Transf.*, 1987, vol. 30, pp. 2161–70.
17. W.D. Bennon and F.P. Incropera: *Int. J. Heat Mass Transf.*, 1987, vol. 30, pp. 2171–87.
18. S. Asai and I. Muchi: *Trans. Iron Steel Inst. Jpn.*, 1978, vol. 18, pp. 90–98.
19. H.T. Zhang, H. Nagaumi, Y.B. Zuo, and J.Z. Cui: *Mater. Sci. Eng. A*, 2007, vol. 448, pp. 189–203.
20. B.E. Launder and B.I. Sharma: *Lett. Heat Mass Transf.*, 1974, vol. 1, pp. 131–37.
21. E.K. Jensen: in *Light Metals 1980*, TMS, Warrendale, PA, 1980, pp. 631–42.
22. G.U. Grün, I. Eick, and D. Vogelsang: in *Light Metals 1994*, TMS, Warrendale, PA, 1994, pp. 863–68.
23. Y. Watanade and N. Hayashi: in *Light Metals 1996*, TMS, Warrendale, PA, 1996, pp. 979–84.
24. M.A. Wells, D. Li, and S.L. Cockcroft: *Metall. Mater. Trans. B*, 2001, vol. 32B, pp. 929–39.
25. R. Abid: *Int. J. Eng. Sci.*, 1993, vol. 31, pp. 831–40.
26. M.G. Chu and D.A. Granger: *Mater. Sci. Forum*, 1996, vols. 217–222, pp. 1505–10.